



HAL
open science

Impact of n -type doping on the carrier dynamics of silicon nanowires studied using optical-pump terahertz-probe spectroscopy

Alexandre Beaudoin, Bassem Salem, Thierry Baron, Pascal Gentile, Denis Morris

► **To cite this version:**

Alexandre Beaudoin, Bassem Salem, Thierry Baron, Pascal Gentile, Denis Morris. Impact of n -type doping on the carrier dynamics of silicon nanowires studied using optical-pump terahertz-probe spectroscopy. *Physical Review B: Condensed Matter and Materials Physics (1998-2015)*, 2014, 89 (11), pp.115316. 10.1103/PhysRevB.89.115316 . hal-01798486

HAL Id: hal-01798486

<https://hal.science/hal-01798486>

Submitted on 28 Sep 2022

HAL is a multi-disciplinary open access archive for the deposit and dissemination of scientific research documents, whether they are published or not. The documents may come from teaching and research institutions in France or abroad, or from public or private research centers.

L'archive ouverte pluridisciplinaire **HAL**, est destinée au dépôt et à la diffusion de documents scientifiques de niveau recherche, publiés ou non, émanant des établissements d'enseignement et de recherche français ou étrangers, des laboratoires publics ou privés.



Impact of n -type doping on the carrier dynamics of silicon nanowires studied using optical-pump terahertz-probe spectroscopy

A. Beaudoin

Institut interdisciplinaire d'innovation technologique (3iT), Centre de recherche en nanofabrication et nanocaractérisation (CRN²), Université de Sherbrooke, Sherbrooke, Québec, Canada J1K 2R1

B. Salem and T. Baron

Laboratoire des Technologies de la Microélectronique (LTM), UMR 5129 CNRS-UJF, CEA Grenoble, 17 Rue des Martyrs, F-38054 Grenoble, France

P. Gentile

SiNaPS Laboratory SP2M, UMR-E CEA/UJF-Grenoble 1, INAC, F-38054 Grenoble, France

D. Morris*

Institut interdisciplinaire d'innovation technologique (3iT), Centre de recherche en nanofabrication et nanocaractérisation (CRN²), Université de Sherbrooke, Sherbrooke, Québec, Canada J1K 2R1 and Laboratoire Nanotechnologies Nanosystèmes (LN2), CNRS UMI-3463, Université de Sherbrooke, 3000 Boulevard Université, Sherbrooke, Québec, Canada J1K 0A5

(Received 2 January 2014; published 25 March 2014)

The n -doped and undoped silicon nanowires grown by chemical vapor deposition on quartz substrate were characterized using optical-pump terahertz-probe transmission experiments. Temporal decays of the differential transmission measurements are reproduced using a biexponential function with an initial photocarrier lifetime of ~ 2 ps and a longer decay time of 10 ps to a few tens of picoseconds. Based on the influence of the laser fluence, a carrier capture and recombination scenario is proposed to explain these temporal decay curves. For both samples, the capture of photocarriers by the traps present on the surface of the nanowires plays an important role in the observed photoconductivity dynamics. Frequency-dependent complex photoconductivity data curves are extracted from the terahertz (THz) traces taken at different optical-pump THz-probe delays. These data curves are reproduced using a plasmon resonance model. The fitting procedure allows us to determine carrier scattering times of about 28 ± 6 and 14 ± 4 fs for the undoped and doped samples, respectively. Our results show that defects and ionized impurities introduced by n doping the silicon nanowires reduce the photocarrier mobility and lifetime.

DOI: [10.1103/PhysRevB.89.115316](https://doi.org/10.1103/PhysRevB.89.115316)

PACS number(s): 78.67.Uh, 73.63.-b, 78.47.D-

I. INTRODUCTION

Possibilities of growing high-quality semiconductor nanowires (NWs) have opened a whole new spectrum of technological applications and fundamental studies. These NWs are of special interest because of their high surface-to-volume ratio, vertical integration possibilities, and wafer-scale fabrication methods. Obvious complementary metal-oxide semiconductor compatibility motivates the study of silicon nanowires (SiNWs), which can be fabricated through both top-down [1] and bottom-up [2–4] approaches. SiNWs grown by chemical vapor deposition (CVD) have attracted considerable attention for their potential integration into electronic devices [5,6], biological and chemical sensors [7], and photovoltaic devices [8]. Development of such SiNW-based devices still requires a better control of the doping level and a deeper understanding of its influence on the electrical properties of these nanostructures. The reduced dimension of the SiNWs is known to play a role on the dopant incorporation and activation [4]. On the other hand, charge trapping effects at the surface of the NWs induce band bending and affect their

conductivity as well as the photocarrier dynamics [4,9]. It is thus important to address these important issues.

Contact wafer-gated electrical and electro-optical methods [10–12] have already been employed to characterize carrier transport properties of single NWs. The advance of noncontact measurements involving pulsed terahertz (THz) radiation presents great interest for characterizing electrical properties of a large ensemble of nanowires. Recent reports show the use of optical-pump terahertz-probe (OPTP) and terahertz absorption experiments to study the conductivity and carrier dynamics in Ge NWs [13], SnO₂ NWs [14], and III–V NWs [15–19]. OPTP experiments have also been used to study ultrafast conduction dynamics in Si nanocrystal films [20]. Large SiNWs, with diameters varying from 200 to 350 nm, were found to exhibit a photocarrier lifetime on the order of 0.7 ns [21]. For SiNWs having diameters smaller than 100 nm, ultrafast carrier recombination processes associated with surface mid-gap trap states were evidenced [22]. An indirect measure of the recombination rate at the surface of single SiNWs, with diameters ranging from 30 to 120 nm, has been obtained through photocurrent experiments performed under quasi-point-source illumination [12]. Complex conductivity tensors in small SiNWs (diameter of 90 nm) have been determined using THz time-domain spectroscopy measurements [23], but the photoconductivity dynamics has

*Author to whom correspondence should be addressed: denis.morris@usherbrooke.ca

not been studied yet in these small-diameter SiNWs using OPTP experiments.

In this paper, we demonstrate the influence of dopant incorporation on photoconduction dynamics in SiNWs with small diameters using noncontact optical measurements. Our results show that defects and ionized impurities introduced by n doping the CVD-grown silicon nanowires tend to reduce the photoexcited carrier lifetime and degrade their conductivity properties. Moreover, we show that the photocarrier density and the carrier doping concentration can be assessed using a Drude-plasmon model.

II. EXPERIMENT

The n -doped and nonintentionally doped (designated as undoped) silicon nanowires were grown using a vapor-liquid-solid (VLS) mechanism on quartz substrates. The substrates were previously ultrasonically cleaned in acetone and rinsed with isopropanol (IPA). This was immediately followed by the deposition of a 2-nm-thick gold layer in a vacuum pressure of 10^{-6} Pa. For the undoped sample, the growth step was performed in a horizontal low-pressure chemical vapor deposition (LPCVD) reactor at 600°C (at 650°C for the n -doped sample) at a total pressure of 3 Torr using SiH_4 as the Si source, HCl gas to inhibit the gold diffusion and two-dimensional (2D) growth, and hydrogen (H_2) as the carrier gas (1.9 standard liters per minute). The electrical properties of nanowires grown under such conditions present a p -type semiconductor behavior [10] with an estimated density of ionized acceptors of around 10^{15} cm^{-3} . n -type doping is achieved by introducing phosphine (PH_3) in the reactor, with a $p\text{PH}_3/p\text{SiH}_4$ ratio equal to 10^{-3} . According to our calibration curve, which is based on previous electrical measurements done on a few individual NWs [24], such a phosphine gas pressure should give rise to a doping level of about 4×10^{18} impurities/ cm^3 .

Scanning electron micrographs (SEM) of the n -doped and undoped samples (see Fig. 1) show a dense array of uniform cylindrical shaped SiNWs with no privileged growth alignment since the quartz crystallographic structure does not match that of silicon. For the n -doped sample, we find a distribution of NWs with a mean length of $8 \pm 3\ \mu\text{m}$, a mean diameter of $90 \pm 40\text{ nm}$, and a density of $1.7 \pm 0.4\ \text{NWs}/\mu\text{m}^2$. For the undoped sample, we find slightly bigger nanowires with a mean length of $12 \pm 3\ \mu\text{m}$ and a mean diameter of $110 \pm 60\text{ nm}$ but with a reduced density of about $0.9 \pm 0.3\ \text{NWs}/\mu\text{m}^2$. The different NW dimensions observed for the two samples are believed to be related to the difference in the growth conditions: it seems that the gold dewetting process performed at 650°C for the n -doped sample gave rise to smaller gold nanoparticles at a higher density.

A Ti:sapphire regenerative amplifier was used as the excitation source for the time-resolved photoconductivity measurements. This source delivers 70-fs laser pulses with a central wavelength of 800 nm at a 1-kHz repetition rate. The output power of the laser source is limited to 300 mW. The laser beam was split into three distinct beams: (i) a pump beam used to create photocarriers in the SiNW samples, (ii) an excitation beam used to generate the THz-probe beam, and (iii) a probing beam used to detect THz pulses transmitted through the SiNW

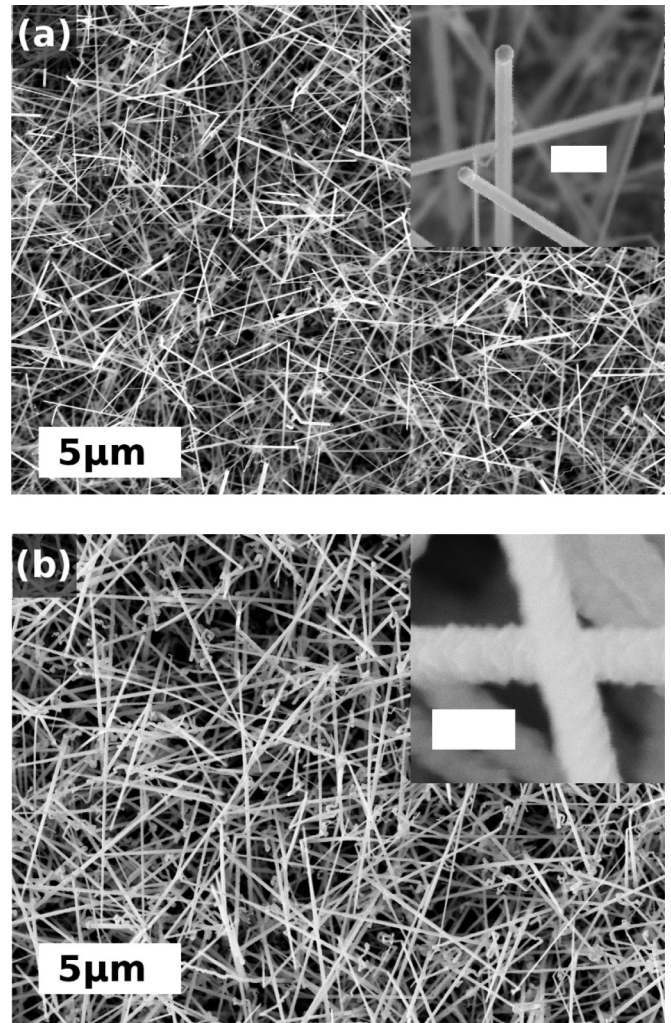


FIG. 1. Scanning electron micrographs of the (a) n -doped and (b) undoped SiNWs samples taken at normal incidence. The inset in (a), with a scale bar of 500 nm, shows two nanowire tips. The inset in (b), with a scale bar of 200 nm, shows the roughness of the NW surface.

samples. The optical-pump beam is polarized parallel to the THz-probe beam. An 80-mW excitation beam was used to generate the THz-probe beam by optical rectification in a $10\text{ mm} \times 10\text{ mm}$ and 1-mm-thick ZnTe crystal. The THz radiation was focused on the sample surface on a spot diameter of about 2.7 mm using a parabolic mirror. A maximum power of 30 mW on a spot 5.9 mm in diameter ($1/e^2$ width) was used for the optical-pump beam. Assuming a spatial Gaussian profile, this laser excitation gives a mean laser fluence, over the THz spot area on the sample, of $F_0 = 360 \pm 60\ \mu\text{J}/\text{cm}^2$ per pulse. The transmitted THz pulses were detected using electro-optic sampling in a 0.5-mm-thick ZnTe crystal. The OPTP measurements were obtained using two delay lines (for the pump and probe beams). Pump-induced changes were measured at the peak of the transmitted THz pulse. The optical-pump beam and the THz-probe beam were chopped at 10 and 455 Hz, respectively, and a double-modulation technique with two lock-in amplifiers was used in order to extract the photoconductivity signal of the NW samples.

Measurements were performed at room temperature in a dry nitrogen atmosphere.

III. RESULTS AND DISCUSSION

A. Conductivity

An appropriate modeling of the THz pulse transmission through a given sample is key to reasonable calculations of its dielectric properties. In this study, THz pulses are perpendicularly incident on a film of randomly oriented NWs. The NW film can be considered thick if the echoes of the main THz pulse coming from back and forth reflections on the film interfaces show no temporal overlap. A film of thickness d with real part of the refractive index n will have its echoes separated by $2dn/c$ seconds, where c is the speed of light. For $n = 3$ and $d = 10 \mu\text{m}$, echoes are separated by ~ 0.1 ps such that the main THz pulse will be combined with those echoes. Under these conditions, which prevail for this study, we can use a thin-film transmission model to extract the dielectric properties of our NW films. This model is described in Appendix A.

Equations (A1) and (A2) have been used to determine the real and imaginary parts of the refractive index. The effective film thickness is required for this calculation. The upper thickness value should be $\sim 10 \mu\text{m}$, which corresponds to the case of vertically aligned NWs. However, the SEM images (Fig. 1) of our samples show that most of the NWs are inclined relative to the surface normal. Using these images, a direct estimation of the mean travel distance through a stack of inclined NWs is not possible. Moreover, each NW has a different contribution to the absorption signal. Indeed, THz absorption by a given NW depends on its orientation relative to the linear polarization of the THz beam, which is parallel to the surface in our experiments. Therefore, an empirical method was used to extract the effective film thickness. This is done by using the THz absorption measurements for the n -doped sample. Details of this method are given in the following paragraph.

The calculated complex refractive index of the n -doped sample at 1 THz as a function of the NW film thickness is shown in Fig. 2(a). In order to reproduce the phase shift and the attenuation of the THz pulses that pass through the NW film, both the real and imaginary parts of the refraction index (n and k) have to increase as the effective film thickness decreases. The expected refractive index can be estimated using a linear combination of air and silicon refractive indexes weighted by their respective surface coverage. The reported value for the refractive index of undoped bulk Si at 1 THz is 3.4174 [25] and does not change significantly for a doped Si substrate [26]. By considering a filling factor of 0.90 ± 0.05 , the expected effective refractive index of our NW films should be 3.2 ± 0.1 . An empirical film thickness of $d = 1.4 \pm 0.2 \mu\text{m}$ can then be obtained using the data curve in Fig. 2(a). This empirical method cannot be used for the undoped sample due to the small absorption signal. Since both samples show comparative SEM images, we assume the same effective film thickness for the undoped NW sample.

Figure 2(b) shows the complex refractive index values of the n -doped sample as a function of frequency. These values were calculated using an effective film thickness of $1.4 \mu\text{m}$.

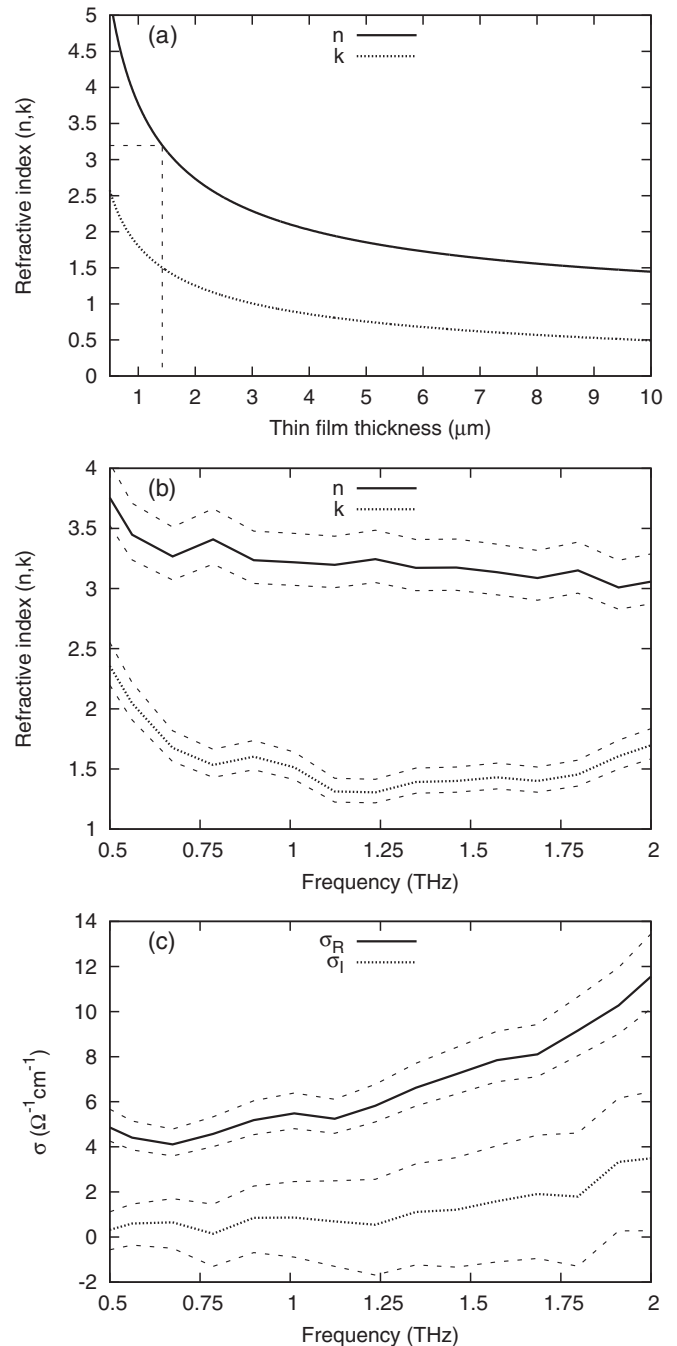


FIG. 2. (a) Complex refractive index ($\tilde{n} = n + ik$) extracted at 1 THz as a function of thin-film thickness. An effective value of $n = 3.2$ is expected given the areal filling factor of bulk Si and air in our NW films. The corresponding thickness of $1.4 \mu\text{m}$ is indicated by a dashed line. (b) Complex refractive index calculated using a film thickness of $1.4 \mu\text{m}$. (c) Complex conductivity values calculated using the same film thickness and $\epsilon_\infty = (3.1 \pm 0.1)^2$ as determined by the refractive index at 2 THz. The dashed lines in (b) and (c) correspond to values obtained using a thickness uncertainty of $\pm 0.2 \mu\text{m}$.

The dashed curves obtained for film thicknesses of 1.2 and $1.6 \mu\text{m}$ illustrate the range of uncertainties for both the real and imaginary parts of the refractive index. Values of n and k vary by 20% and 85%, respectively, in the frequency range between

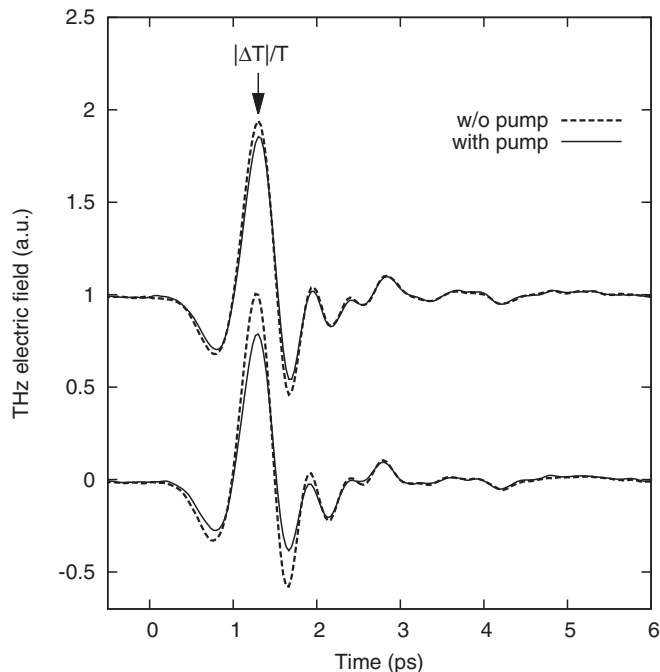


FIG. 3. Effect of optical pumping at maximum fluence on the THz waveform for both samples. Data points for the n -doped sample were vertically shifted above undoped data points for clarity. OPTP measurements, shown in Fig. 4, were taken at the position corresponding to the maximum THz signal (indicated by the arrow).

0.5 and 2 THz. The complex conductivity calculated using those values is shown in Fig. 2(c). These calculations were performed using a relative permittivity at high frequencies of $(3.1 \pm 0.1)^2$. The real part of the conductivity is positive and increases with frequency, whereas the imaginary part presents an uncertainty too important for a reasonable determination of its sign. We were not able to fit these experimental data with any simple known transport models such as Drude or Drude plasmon [27]. This issue is certainly related to the difficulty to modelize the transmission of a THz pulse through a distribution of randomly oriented NWs.

B. Time-resolved photoconductivity

Figure 3 shows the THz pulses transmitted through both samples with and without the optical pump at maximum fluence. For both samples, the amplitude of the transmitted pulse is reduced when optically pumped. The absence of a temporal shift between the pump-on and pump-off THz pulses indicates that optical pumping does not change the refractive index of the substrate. The relative pump-induced change in the transmission signal is defined as follows: $\Delta T/T = (T_{\text{pump}} - T_{\text{w/o pump}})/T_{\text{w/o pump}}$. These changes are about -20% and -10% for the undoped and n -doped samples, respectively. The evolution of these values as a function of the pump-probe delay were recorded for OPTP measurements. In the limit of small THz absorption we consider a time-dependent differential signal given by $\Delta T(t)/T \propto \Delta\sigma(t) = e[\mu_n(t)\Delta n(t) + \mu_p(t)\Delta p(t)]$. The photoconductivity $\Delta\sigma(t)$ depends on the change in the density of electrons $[\Delta n(t)]$ and holes $[\Delta p(t)]$ in excess in the SiNWs. After a fast relaxation time of typically

a few hundreds of femtoseconds, the carrier mobility can often be considered a time-independent quantity.

OPTP results obtained for the undoped NW sample are shown in Fig. 4(a). For all laser fluences, a steep rise in signal is observed for the first 400 fs followed by a quasiexponential decay over a few tens of picosecond. The bump observed at 10.5 ps is caused by extra photocarriers generated in the NWs by the residual optical-pump pulse that is reflected on the back substrate-air interface (the quartz substrate is 1 mm thick). The expression used to reproduce the temporal data curves will be discussed below. The level of optically pump-induced absorption of the THz pulses by the nanowires depends on the laser fluence. The differential transmission signal $\Delta T/T$ is negative, with a maximum absolute value of 3% for the lowest fluence ($F_0/10$). The $|\Delta T_{\text{max}}|/T$ values shown in the inset vary sublinearly with the fluence: it reaches 20% for the highest fluence (F_0). No change in the optical properties of the quartz substrate was measured over the range of laser fluences covered in this study. The layer of randomly oriented NWs causes significant light scattering, so it is difficult to estimate the total sample absorption at 800 nm. However, it is reasonable to assume that the number of photocarriers generated in the NWs varies linearly with the pump fluence. Therefore, the sublinear fluence-dependent $|\Delta T_{\text{max}}|/T$ behavior shown in the inset is believed to be related to a change in the carrier transport properties as the density of photocarriers increases. This behavior is compatible with a plasmonlike response.

Temporal data curves obtained for the n -doped NW sample are plotted in Fig. 4(b). The different temporal data curves show a rapid rise of the OPTP signal followed by biexponential decay behavior. The amplitude of the differential transmission signal $|\Delta T|/T$ is smaller for this sample. Considering the reduced signal-to-noise ratio, we thus limit our study down to a laser fluence of $F_0/4$ ($90 \mu\text{J}/\text{cm}^2$ per pulse). At this fluence, the OPTP signal is reduced by a factor of 3.6 in comparison with the undoped NW sample. This factor is larger than the difference in the excited volume of NWs deduced from the scanning electron micrographs: the total volume of SiNWs is found to be only about 20% higher for the undoped sample. Moreover, the maximum differential transmission signal increases linearly with the laser fluence for this n -doped sample [see the linear regression in the inset of Fig. 4(a)]. The reduced OPTP signal is explained by the fact that (i) ionized dopants add extra scattering mechanisms and (ii) free electrons open extra recombination mechanisms. The following equation was used to fit the temporal data curves of Fig. 4:

$$\frac{|\Delta T(t)|}{T} = f(t) + a_R \times f(t - t_{0R}),$$

$$f(t) = \text{erfc}\left(\frac{-t}{\tau_c}\right) \left[a_1 \exp\left(\frac{-t}{\tau_1}\right) + a_2 \exp\left(\frac{-t}{\tau_2}\right) \right] \quad (1)$$

In this expression, τ_1 and τ_2 correspond to two characteristic decay times of the OPTP signal, while τ_c corresponds to the signal rise time. The amplitudes a_1 and a_2 represent the contribution from each temporal decay component. The artifact caused by the reflection of the optical-pump pulses on the back surface of the substrate is taken into account by adding a simple replica to the simulated temporal data curves. This replica is delayed in time by a value t_{0R} and weighted by a coefficient a_R .

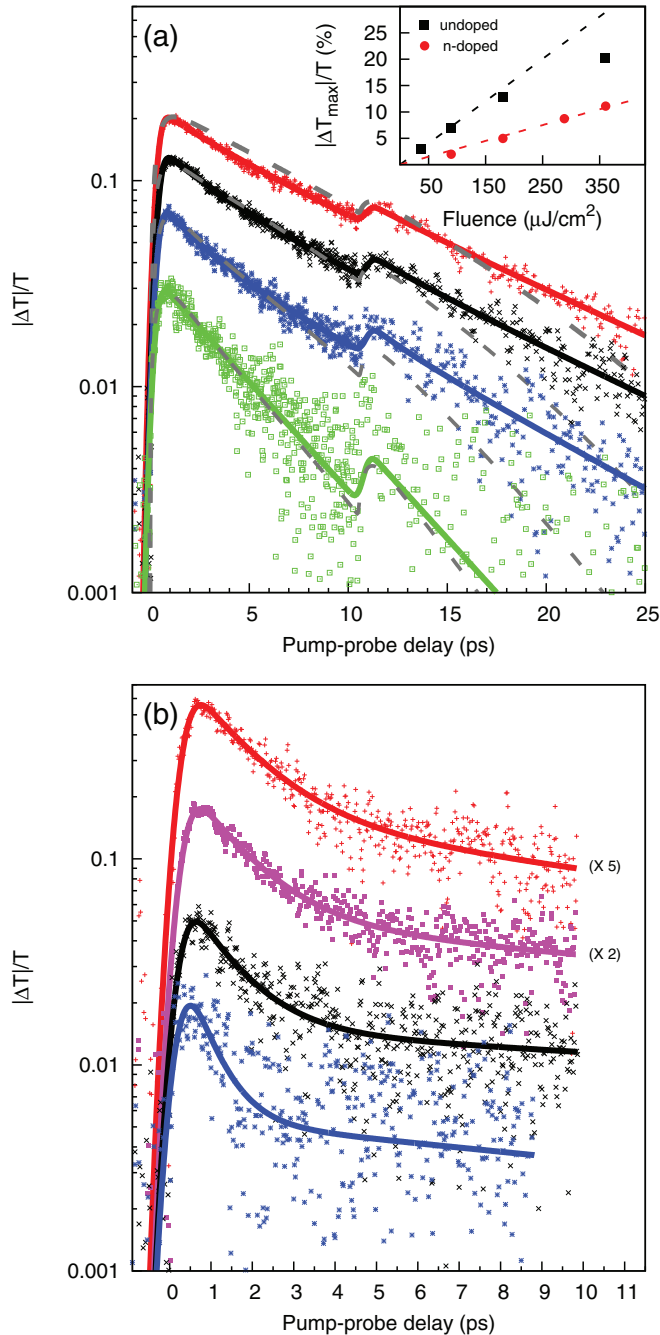


FIG. 4. (Color) Optical-pump THz-probe measurements obtained for (a) undoped and (b) n -doped SiNW samples at different laser fluences. Red: $F_0 = 360 \mu\text{J}/\text{cm}^2$, magenta: $F_0/1.25$, black: $F_0/2$, blue: $F_0/4$, and green: $F_0/10$. For clarity, the upper two temporal data curves in (b) are stretched vertically using scaling factors of 5 and 2, respectively. The solid lines correspond to the best fits of the temporal data curves using a biexponential decay function, except for the green line, which corresponds to the best fit using a single exponential decay function. The four dashed gray lines in (a) are obtained via a single fitting procedure using a rate equations model with fluence-dependent carrier capture time and mobility terms. The inset in (a) shows the maximum differential transmission data plotted as a function of the fluence for both the undoped and the n -doped NW samples. Dotted lines show sublinear and linear dependence with fluence for the undoped and n -doped samples, respectively.

TABLE I. Parameters used to fit the temporal data curves (solid lines in Fig. 4). Fixed parameters are t_{0R} , τ_c , and a_R .

Fluence ($\mu\text{J}/\text{cm}^2$ per pulse)	τ_1 (ps)	τ_2 (ps)	a_1/a_2
Undoped sample			
$F_0 = 360 \pm 60$	3 ± 1	10 ± 1	0.3 ± 0.1
$F_0/2$	3 ± 1	9 ± 2	0.5 ± 0.1
$F_0/4$	2 ± 1	8 ± 2	0.6 ± 0.1
$F_0/10$	4 ± 1		
n -doped sample			
F_0	1.4 ± 0.5	16 ± 10	3.7 ± 0.5
$F_0/1.25$	1.3 ± 0.3	25 ± 15	3.7 ± 0.7
$F_0/2$	1.1 ± 0.4	37 ± 20	3.7 ± 0.5
$F_0/4$	0.6 ± 0.2	21 ± 15	5 ± 2

The colored solid lines plotted in Fig. 4 are the best fits through the experimental data points. These fitting curves are obtained with $t_{0R} = 10.5$ ps, $\tau_c = 0.37$ ps, and $a_R = 0.075$. A few iterations of the fitting procedure showed small variations for those parameters and were thus kept constant. Values obtained for the adjustable parameters are given in Table I.

For the n -doped sample, the photoconductivity dynamics is dominated by an ultrafast-decay component partly related to the capture and nonradiative recombination of holes by the negatively charged traps (deep-level defects) present on the surface of the NWs and partly due to the recombination of holes with free electrons within the core of the nanowires (most likely Auger-type recombination mechanism). The short decay time (~ 1 ps) is much smaller than the recombination time reported for bulk silicon [28]. The longer-time-decay component, characterized by a typical decay time value of ~ 20 ps, must then be related to the capture of the remaining photoelectrons. This photocarrier capture and recombination scenario is illustrated in the schematic of Fig. 5(a). Large uncertainties are found on the extracted long-decay-time value due to decreasing signal-to-noise ratio with pump-probe delay times. As the laser fluence increases, our results show a slight increase of the τ_1 values and a constant a_1/a_2 ratio. The photocarrier dynamics is thus nearly fluence independent for this n -doped NW sample since holes get trapped and/or recombine rapidly at all fluences.

For the undoped NW sample, excited at the lowest laser fluence ($F_0/10$), a single exponential decay function with $\tau \sim 4$ ps can be used to fit the temporal decay behavior. At higher fluences, the fit quality is improved by using a biexponential function. The contribution from the long-decay-time component is found to increase with fluence. Moreover, the effective decay time gets longer at high fluences. These observations can be explained by time-dependent capture mechanisms, as sketched in the diagram of Fig. 5(b). Note that the surface-depleted field should be reduced in this undoped sample. At the lowest fluence, the initial capture of photoelectrons by the traps present on the surface of the NWs is rapidly followed by hole capture and recombination mechanisms. A gradual saturation of trap states is expected as the fluence increases. These effects tend to slow down the photocarrier capture and recombination mechanisms. Jepsen *et al.* [28] have used a set of rate equations with a saturable trapping time to fit OPTP measurements performed on microcrystalline silicon

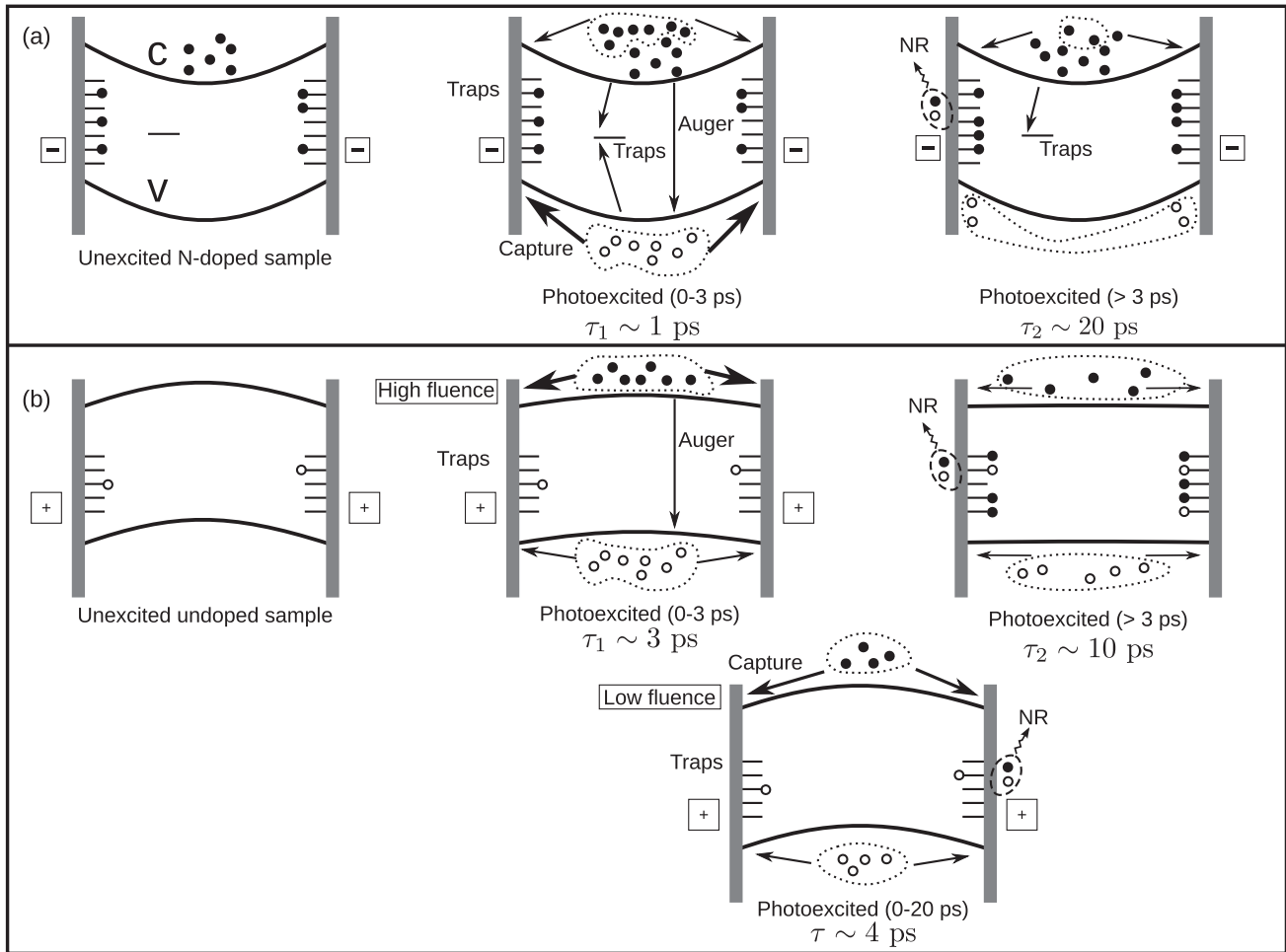


FIG. 5. Scenario of photocarrier capture/recombination dynamics proposed for the (a) *n*-doped and (b) undoped NW samples. For *n*-doped NWs, band bending is due to negatively charged surface traps (deep-level defects). The density of traps in these NWs is such that photoexcitation and the trap-filling effect have only a weak influence on the surface-depleted field. At short pump/probe delays (0 to 3 ps), mobile photocarriers rapidly disappear (in ~ 1 ps) via competitive mechanisms, indicated by arrows. At longer delays, the remaining photoelectrons, confined in the core of the NWs, will take a much longer time to be captured by trap states. The nonintentionally doped NWs are, in fact, slightly *p* doped: band bending results from positively charged surface traps. The density of traps in these NWs seems to be small enough to observe a significant reduction of the surface-depleted field through photoexcitation (at high laser fluence) and the trap-filling effect. For both samples, nonradiative (NR) electron-hole recombination processes can take place on the various traps.

samples. In the present study, the photocarrier dynamics can be fitted using a similar set of equations, but a fluence-dependent mobility term was necessary in order to obtain a reasonable fit. This rate equation model with saturable traps contains four key fitting parameters: a carrier cooling time τ_c , a capture time obtained for unoccupied traps $\tau_{\text{trap}0}$, a carrier recombination time τ_{rec} , and R , a trap filling factor corresponding to the ratio between the number of photoinjected carriers at the highest fluence and the number of surface traps. The rate equations are given in Appendix B. The carrier cooling time τ_c and the minimal trapping time $\tau_{\text{trap}0}$ are respectively kept at 0.37 and 4 ps. These values are deduced from the biexponential fitting procedure. We use the relative $|\Delta T_{\text{max}}|/T$ values taken from Fig. 4(a) to account for the fluence-dependent mobility term. A reasonable fit of the four temporal data curves [gray dashed lines shown in Fig. 4(a)] is obtained using a constant recombination time τ_{rec} equal to 10 ± 1 ps and a trap filling factor R of 10 ± 2 . A value of $R > 1$ indicates that there are

enough photocarriers to completely saturate the surface trap states at the highest fluence. A crude experimental estimation for the fraction of photons absorbed by the NWs (about 10%) leads to an areal density of single charged traps of $\sim 6 \times 10^{12} \text{ cm}^{-2}$, which is consistent with the value of $\sim 1.7 \times 10^{13} \text{ cm}^{-2}$ reported for unpassivated silicon nanowires [29].

In an optical-pump THz-probe experiment both types of photocarriers (excess electrons and holes) contribute to the differential transmission signal. For the undoped NW sample, results indicate that both types of carriers are captured in a characteristic time of ~ 4 ps at low fluence and up to ~ 10 ps at the highest fluence. For the *n*-doped NW sample, the a_1/a_2 value of ~ 3.7 (see Table I) indicates that a large portion of the photoinjected carriers (both electrons and holes) become inactive in a characteristic time of ~ 1 ps. Different mechanisms can explain the smaller decay-time value observed for this *n*-doped sample [see Fig. 5(a)]: (i) *n* doping the SiNWs might add extra nonradiative recombination

centers, (ii) Auger recombination processes are more favorable at higher doping levels, and (iii) carrier capture by the surface trap states might be sped up by the electric field present in the carrier-depleted region near the NW surface. On the other hand, the longer-decay-time component, with a characteristic decay-time value of a few tens of picoseconds, is attributed to the capture of the remaining electrons most likely confined in the center of the nanowires owing to the surface depleted field. Finally, the maximum differential transmission signal is reduced by a factor of 3.6 (compared with the value obtained for the undoped sample) at a fluence of $90 \mu\text{J}/\text{cm}^2$ per pulse. This result is attributed mainly to a reduction of photocarrier mobility caused by scattering on ionized n -type dopants.

C. Frequency-dependent photoconductivity

The frequency-dependent complex photoconductivity extracted from the THz absorption taken at three different pump-probe delays is shown in Fig. 6 for frequencies ranging from 0.5 to 2.0 THz, with the signal-to-noise ratio being too low outside this frequency range. Calculations were performed with a thin-film photoconductivity model [30] using a $1.4\text{-}\mu\text{m}$ film thickness. For the undoped sample, the real part of photoconductivity is about 10 S/cm at 1 THz. For the n -doped sample, this value is reduced by a factor of 2. For both samples, the real part of the photoconductivity is found to be constant or slightly increasing with frequency, whereas the imaginary part is negative for both samples. These trends are compatible with a Drude-plasmon conductivity model. The absolute values of the real and imaginary parts of photoconductivity are found to

decrease as the pump-probe delay increases. This behavior is consistent with a decreasing number of mobile charges.

Despite noisy extracted data points in the photoconductivity values, the observed behaviors are sufficiently close to those expected for a plasmon-type conductivity to justify an attempt at fitting these curves. A modified Drude-plasmon conductivity expression [19], described in Appendix C, was used to fit the results for both samples. The fitting parameters are the photocarrier density N , the doping carrier density N_d , the average carrier scattering time τ , and a geometrical factor f that depends on the polarization of the THz-probe beam relative to the mean NW orientation (see the description in Appendix C).

For the undoped NW sample, N_d is set to zero, and the other parameters were found by simultaneously fitting every data set. Extracted values are $f = 0.2$, $\tau = 28 \pm 6 \text{ fs}$, and photocarrier densities $N(t_{\text{max}}) = (7.7 \pm 0.8) \times 10^{17} \text{ cm}^{-3}$, $N(t_1) = (6.5 \pm 0.5) \times 10^{17} \text{ cm}^{-3}$, and $N(t_2) = (3.3 \pm 0.3) \times 10^{17} \text{ cm}^{-3}$ at the three marked pump-probe delays. The temporal evolution of the photocarrier density, deduced from this fitting procedure, is consistent with the characteristic capture/recombination time obtained previously.

For the n -doped NW sample, the fitting procedure is slightly different. The photoconductivity is lower such that some parameters had to be fixed to obtain realistic fits. If the two samples are structurally similar, we can reasonably fix $f = 0.2$. The total injected numbers of photocarriers per NW are also similar. However, the capture/recombination time is found to be smaller in n -doped NWs, giving rise to a reduced photocarrier density at all pump-probe delays (compared to those of the undoped sample). At the delay corresponding

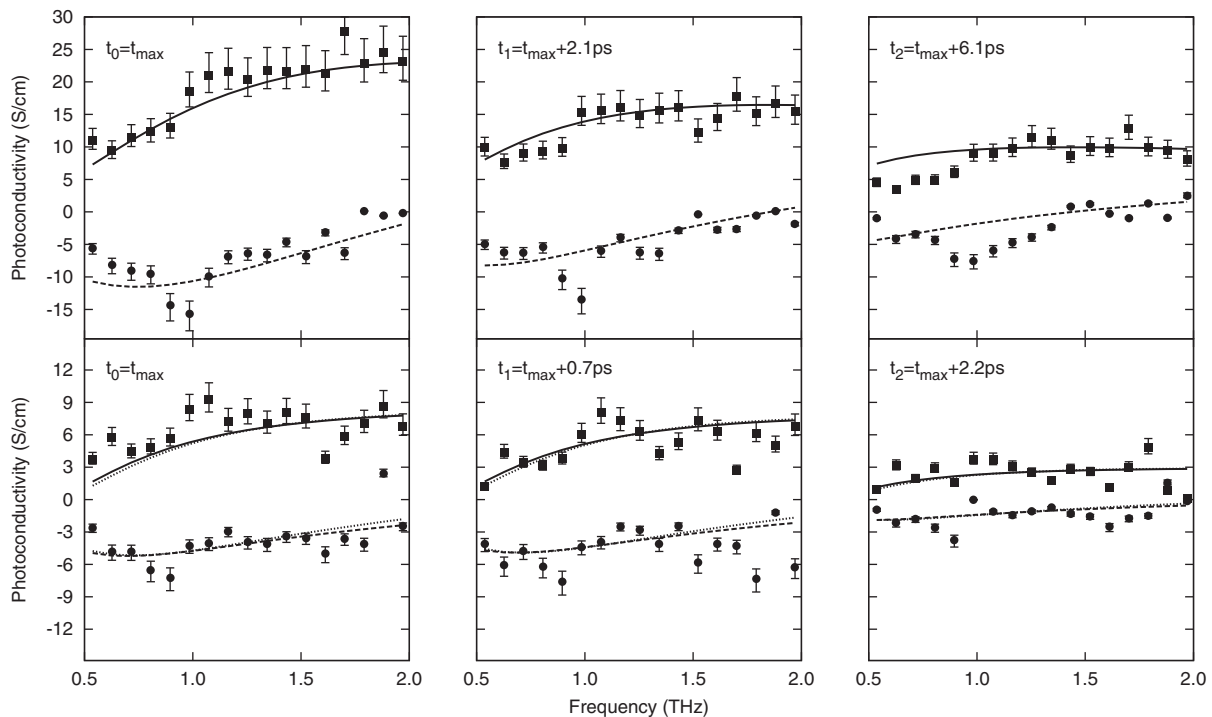


FIG. 6. Real (squares) and imaginary (circles) components of the photoconductivity extracted from the THz absorption measurement taken at three different pump-probe delays for the undoped (top row) and n -doped (bottom row) NW samples. A pump-probe delay close to $\Delta T_{\text{max}}/T$ is labeled t_{max} . The solid and dashed lines show the real and imaginary parts of the fitting procedure, respectively. For the n -doped sample, dotted lines represent deviations of the fit if the lower initial value of the photocarrier density is used instead of the upper bound. Error bars show the thin-film thickness uncertainty effect on extracted photoconductivity.

to the maximum photoconductivity signal, the photocarrier density is then fixed at either an upper value of $N = 7.7 \times 10^{17} \text{ cm}^{-3}$ or at a lower value of $N = 4.2 \times 10^{17} \text{ cm}^{-3}$. The latter value was estimated using the $|\Delta T_{\text{max}}|/T$ ratio between undoped and n -doped samples at maximum fluence. The doping carrier density is used as an adjustable parameter. Using those photocarrier density boundaries, a range of values has been obtained for each fitting parameter and is added to the uncertainty. The set of values extracted using this fitting procedure contains a carrier scattering time of $\tau = 14 \pm 4$ fs, a doping carrier density of $N_d = (5 \pm 3) \times 10^{17} \text{ cm}^{-3}$, and photocarrier densities of $N(t_1) = (5.6 \pm 1.6) \times 10^{17} \text{ cm}^{-3}$ and $N(t_2) = (2.1 \pm 0.6) \times 10^{17} \text{ cm}^{-3}$. Values obtained for photocarrier densities are again consistent with those expected when considering a photocarrier lifetime of 1.4 ps (as previously determined). Uncertainty on N_d is relatively large ($\sim 60\%$), but the extracted doping carrier concentration is an order of magnitude less than what was measured using electrical measurements on a few individual NWs. Since the resistivity is found to vary significantly from one NW to the other, the noncontact OPTP measurements and the fitting procedure described above are believed to be a better way to estimate the average doping concentration over a large ensemble of nanowires.

The Drude carrier mobility, $\mu = e\tau/m^*$, calculated from the carrier scattering time values is estimated to be around $190 \pm 40 \text{ cm}^2/\text{V s}$ for the undoped NWs and $95 \pm 25 \text{ cm}^2/\text{V s}$ for the n -doped sample. If the photoconductivity is dominated by the electron transport, these mobility values are much smaller than those found for bulk silicon: it is reduced by factors of about 7 and 5 for the undoped and n -doped NWs, respectively. This reduced carrier mobility is attributed to extra scattering with various defects/traps (dangling bonds, Au inclusions, adsorbents) located at the surface of the NWs. The n -doped sample's mobility might be closer to the bulk value due to a larger band bending effectively screening some surface defects.

IV. CONCLUSION

In summary, our results show that OPTP measurements give valuable information on time-resolved photoconductivity properties of silicon nanowires which are elaborated by CVD using a VLS mechanism. The photoconductivity dynamics are well fitted by a biexponential decay function for both the n -doped and the undoped samples, and plausible capture and recombination scenarios are proposed to explain such behaviors. n doping the silicon nanowires is found to reduce photocarrier mobility and lifetime. For the undoped NW sample, a rate equation model with saturable surface traps has been used to reproduce a set of four temporal data curves obtained at different laser fluences, and this analysis gives a reasonable value of $\sim 6 \times 10^{12} \text{ cm}^{-2}$ for the density of traps at the surface of these nanowires. Mobility values, extracted from the frequency-dependent photoconductivity data curves, are smaller (factor of >5) than the bulk Si ones. Further work will aim at improving the photoconductivity properties and mobility of these SiNWs via *in situ* passivation techniques [12] since they seem to be crucial for small-diameter SiNWs.

ACKNOWLEDGMENTS

This work was supported financially by NSERC, CFI, FRQNT (Québec), and Nano-Québec. The authors would like to thank J. F. Allard and M. Bernier for valuable discussions and expert advice on the OPTP measurements, G. Laliberté and F. Francoeur for their technical support, M. Cloutier and G. Rosaz for the scanning electron micrographs, and A. Potié for valuable discussions on the NW growth technique.

APPENDIX A: THIN-FILM TRANSMISSION MODEL

In order to determine the THz absorption of a NW film, a comparison in the frequency domain is made between THz pulse transmission through the substrate (reference) and through the NW film on a substrate (sample). The complex refractive index of the surrounding dry nitrogen atmosphere is denoted n_1 . The NW film (2) and the substrate (3) have their respective complex refractive index (n_2, n_3) and thickness (d_2, d_3). The Fresnel amplitude transmission coefficient from medium a to b is denoted t_{ab} , and the Fabry-Pérot transmission function through a medium y placed between x and z media is written as F_{xyz} . Using this notation, the complex frequency spectrum of the reference (R) and sample (S) THz pulse signals can be written as

$$R(\omega) = E_0(\omega) \exp\left(\frac{-in_1 d_3 \omega}{c}\right) t_{13} \exp\left(\frac{in_3 d_3 \omega}{c}\right) t_{31}, \quad (\text{A1})$$

$$S(\omega) = E_0(\omega) \exp\left(\frac{-in_1(d_2 + d_3)\omega}{c}\right) t_{12} \exp\left(\frac{in_2 d_2 \omega}{c}\right) \times F_{123} t_{23} \exp\left(\frac{in_3 d_3 \omega}{c}\right) t_{31}, \quad (\text{A2})$$

where $E_0(\omega)$ is the frequency content of the THz signal corresponding to pulse propagation through a dry nitrogen atmosphere. Reflections due to substrate are excluded from the measured signal. Light scattering by the nanowires, which are typically $10 \mu\text{m}$ long with diameters of ~ 100 nm, is neglected at THz frequencies. Equations (A1) and (A2) also assume the existence of an effective Fresnel surface, which is a reasonable assumption for dense NW films. For the two studied samples, the NWs covered the substrate with an areal filling factor estimated to 90%.

APPENDIX B: RATE EQUATION MODEL WITH SATURABLE TRAPS

If the photoconductivity signal is dictated by the density of photoelectrons present at the bottom of the conduction band $n_1(t)$, the following set of rate equations can be solved numerically to obtain its time evolution [28]:

$$\frac{dn_2(t)}{dt} = G(t) - \frac{n_2(t)}{\tau_c}, \quad (\text{B1})$$

$$\frac{dn_1(t)}{dt} = \frac{n_2(t)}{\tau_c} - \frac{n_1(t)}{\tau_{\text{trap}}} - \frac{n_1(t)}{\tau_{\text{rec}}}, \quad (\text{B2})$$

$$\frac{dn_{\text{trap}}(t)}{dt} = \frac{n_1(t)}{\tau_{\text{trap}}} - \frac{n_{\text{trap}}(t)}{\tau_{\text{rec}}}, \quad (\text{B3})$$

where $n_2(t)$ corresponds to the density of hot photoelectrons and $n_{\text{trap}}(t)$ represents the density of trapped photoelectrons. The density of hot photoelectrons generated by a Gaussian-like laser pulse is included in the term $G(t)$. The hot photoelectrons relaxation time is designated by τ_c . In this model, the photoelectrons at the bottom of the conduction band can either recombine with holes in a characteristic time τ_{rec} or be captured by trap states in a characteristic time τ_{trap} . For saturable traps, the latter time can be expressed as

$$\tau_{\text{trap}} = \tau_{\text{trap}_0} \left(1 - \frac{n_{\text{trap}}(t)}{n_{\text{t,max}}} \right)^{-1}, \quad (\text{B4})$$

where $n_{\text{t,max}}$ is the density of available trap states and τ_{trap_0} is the initial photoelectron trapping time [with $n_{\text{trap}}(0) = 0$]. A trap filling factor R is defined as

$$R = \frac{\int_{-\infty}^{\infty} G(t) dt}{n_{\text{t,max}}}. \quad (\text{B5})$$

Trap states also empty with a time τ_{rec} . By simultaneously fitting the four curves shown in Fig. 4(a), we extract $\tau_c = 0.37$ ps, $\tau_{\text{trap}_0} = 4$ ps, $\tau_{\text{rec}} = 10 \pm 1$ ps, and $R = 10 \pm 2$. The $n_{\text{t,max}}$ ratio between each fluence data set was fixed to ratios found by considering data shown in the inset in Fig. 4(a) for the undoped sample.

APPENDIX C: PHOTOCONDUCTIVITY MODEL

Photoconductivity $\Delta\sigma$ data shown in Fig. 6 were fitted using the following modified Drude-plasmon conductivity model [19]:

$$\Delta\sigma = \frac{ie^2\omega(N + N_d)}{m^*(\omega^2 - \omega_0^2 + i\omega/\tau)} - \frac{ie^2\omega N_d}{m^*(\omega^2 - \omega_{0d}^2 + i\omega/\tau)}, \quad (\text{C1})$$

$$\omega_0^2 = \frac{fe^2(N + N_d)}{m^*\epsilon}, \quad (\text{C2})$$

$$\omega_{0d}^2 = \frac{fe^2(N_d)}{m^*\epsilon}. \quad (\text{C3})$$

The variables in the model are the electronic charge e and effective mass m^* , the absolute permittivity $\epsilon = \epsilon_r\epsilon_0$, the photocarrier density N , the carrier density resulting from doping N_d , the carrier scattering time, and a geometrical factor f . The latter is related to the relative orientation of the THz pulse polarization and the NW orientation: it is indicative of the magnitude of the depolarization response. An f value between 0 and 1/2 is expected, the latter representing a perpendicular relative orientation of a NW and a THz pulse [15]. For a bulk medium, $f = 0$ and Eq. (C1) gives the classic Drude conductivity. A relative permittivity of $\epsilon_r = (3.1)^2$ was used for the fitting procedure.

-
- [1] Y.-K. Choi, J. Zhu, J. Grunes, J. Bokor, and G. A. Somorjai, *J. Phys. Chem. B* **107**, 3340 (2003).
- [2] W. Lu and C. M. Lieber, *Nat. Mater.* **6**, 841 (2007).
- [3] Y. Wu, Y. Cui, L. Huynh, C. J. Barrelet, D. C. Bell, and C. M. Lieber, *Nano Lett.* **4**, 433 (2004).
- [4] Y. Cui and C. M. Lieber, *Science* **291**, 851 (2001).
- [5] V. Schmidt, J. V. Wittmann, and U. Gösele, *Chem. Rev.* **110**, 361 (2010).
- [6] G. Rosaz, B. Salem, N. Pauc, P. Gentile, A. Poti, and T. Baron, *Microelectron. Eng.* **88**, 3312 (2011).
- [7] Y. Cui, Q. Wei, H. Park, and C. M. Lieber, *Science* **293**, 1289 (2001).
- [8] K. Peng, Y. Xu, Y. Wu, Y. Yan, S.-T. Lee, and J. Zhu, *Small* **1**, 1062 (2005).
- [9] J. Jie, W. Zhang, K. Peng, G. Yuan, C. S. Lee, and S.-T. Lee, *Adv. Funct. Mater.* **18**, 3251 (2008).
- [10] G. Rosaz, B. Salem, N. Pauc, P. Gentile, A. Poti, A. Solanki, and T. Baron, *Semicond. Sci. Technol.* **26**, 085020 (2011).
- [11] T. Richter, H. L. R. Meijers, R. Calarco, and M. Marso, *Nano Lett.* **8**, 3056 (2008).
- [12] Y. Dan, K. Seo, K. Takei, J. H. Meza, A. Javey, and K. B. Crozier, *Nano Lett.* **11**, 2527 (2011).
- [13] J. H. Strait, P. A. George, M. Levendorf, M. Blood-Forsythe, F. Rana, and J. Park, *Nano Lett.* **9**, 2967 (2009).
- [14] X. Zou, J. Luo, D. Lee, C. Cheng, D. Springer, S. K. Nair, S. A. Cheong, H. J. Fan, and E. E. M. Chia, *J. Phys. D* **45**, 465101 (2012).
- [15] P. Parkinson, J. Lloyd-Hughes, Q. Gao, H. H. Tan, C. Jagadish, M. B. Johnston, and L. M. Herz, *Nano Lett.* **7**, 2162 (2007).
- [16] P. Parkinson, H. J. Joyce, Q. Gao, H. H. Tan, X. Zhang, J. Zou, C. Jagadish, L. M. Herz, and M. B. Johnston, *Nano Lett.* **9**, 3349 (2009).
- [17] J. B. Baxter and C. A. Schmittenmaer, *J. Phys. Chem. B* **110**, 25229 (2006).
- [18] H. J. Joyce, J. Wong-Leung, C.-K. Yong, C. J. Docherty, S. Paiman, Q. Gao, H. H. Tan, C. Jagadish, J. Lloyd-Hughes, L. M. Herz, and M. B. Johnston, *Nano Lett.* **12**, 5325 (2012).
- [19] H. J. Joyce, C. J. Docherty, Q. Gao, H. H. Tan, C. Jagadish, J. Lloyd-Hughes, L. M. Herz, and M. B. Johnston, *Nanotechnology* **24**, 214006 (2013).
- [20] L. V. Titova, T. L. Cocker, D. G. Cooke, X. Wang, A. Meldrum, and F. A. Hegmann, *Phys. Rev. B* **83**, 085403 (2011).
- [21] H. Tang, L.-G. Zhu, L. Zhao, X. Zhang, J. Shan, and S.-T. Lee, *ACS Nano* **6**, 7814 (2012).
- [22] A. Kar, P. Upadhyaya, S. Dayeh, S. Picraux, A. Taylor, and R. Prasankumar, *IEEE J. Sel. Top. Quantum Electron.* **17**, 889 (2011).
- [23] M. Lim, S.-J. Choi, G.-S. Lee, M.-L. Seol, Y. Do, Y.-K. Choi, and H. Han, *Appl. Phys. Lett.* **100**, 211102 (2012).
- [24] P. Gentile, A. Solanki, N. Pauc, F. Oehler, B. Salem, G. Rosaz, T. Baron, M. D. Hertog, and V. Calvo, *Nanotechnology* **23**, 215702 (2012).
- [25] J. Dai, J. Zhang, W. Zhang, and D. Grischkowsky, *J. Opt. Soc. Am. B* **21**, 1379 (2004).
- [26] T.-I. Jeon and D. Grischkowsky, *Phys. Rev. Lett.* **78**, 1106 (1997).

- [27] H.-K. Nienhuys and V. Sundström, [Appl. Phys. Lett.](#) **87**, 012101 (2005).
- [28] P. U. Jepsen, W. Schairer, I. H. Libon, U. Lemmer, N. E. Hecker, M. Birkholz, K. Lips, and M. Schall, [Appl. Phys. Lett.](#) **79**, 1291 (2001).
- [29] J. E. Allen, E. R. Hemesath, D. E. Perea, J. L. Lensch-Falk, Z. Y. Li, F. Yin, M. H. Gass, P. Wang, A. L. Bleloch, R. E. Palmer, and L. J. Lauhon, [Nat. Nanotechnol.](#) **3**, 168 (2008).
- [30] H.-K. Nienhuys and V. Sundström, [Phys. Rev. B](#) **71**, 235110 (2005).